

NUMERICAL AND EXPERIMENTAL EVALUATION OF COMPACT TPMS AND OFFSET-STRIP-FIN HEAT EXCHANGERS FOR FUEL CELL SYSTEM COOLING IN AN ELECTRIC AIRCRAFT

Chetan Kumar Sain[1], Sahil Bhapkar[1], Markus Kober[1], Stefan Kazula[1]

[1]German Aerospace Center (DLR) – Institute of Electrified Aero Engines, Cottbus, Germany

Abstract

All-electric propulsion based on fuel cell systems can be used to achieve low-emissions flights in civil aviation. However, reducing the weight and size of the fuel cell system and its critical components is challenging. For regional flights, the fuel cell stacks can require multiple megawatts of heat rejection, necessitating large heat exchangers (HEX) with a significant frontal area, size, and mass. This paper presents a performance study of six compact HEX designs, including two offset-strip-fin plate (OSF) designs and four designs using triply periodic minimal surfaces (TPMS) with embedded coolant channels in the form of pipes and plates. CFD analysis was performed for various air inlet velocities and angles of attack (AoA) to estimate thermal and hydraulic performance. The results were used to calculate HEX size for a system level requirement of 500 kW heat duty. The results show that the modified Gyroid-Pipe-20 design has good combined thermal-hydraulic performance, least losses with tilted angle operation, and moderate cost penalty at system-level combined effect. This design poses challenges for integration inside narrow air ducts and requires air duct optimization. A baseline OSF design with 60 mm length, OSF-Base-60, came out as the best design solution in terms of performance and least pumping power consumption. Not suitable for operation with high AoA, this concept is suitable for Megawatt-Level cooling requirements and can be integrated underneath aircraft in belly-podded configuration with ram air supply. For a nacelle-podded HEX integration, with typically one meter diameter, OSF-AM-60 design, a modified version for additive manufacturing, offers most favorable compromise at system-level assessment. A heat duty of 500 kW can be realized with the OSF-AM-60 with its width under 1 m and a height of 0.6 m, at a moderate penalty against mass and pumping power. Prototypes for OSF-AM-60 and Gyroid-Pipe-20 are under development and in near future, test and validation results will be published.

1. Introduction

The future of civil aviation is to achieve low-emission flights by 2050 [1]. Using an all-electric aircraft with a Low-Temperature Polymer Electrolyte Membrane Fuel Cell propulsion System (LTPEM FCS) could help to achieve this goal. The challenge lies in reducing the weight and size of the LTPEM FCS in order to enable 70-passenger regional flights. The necessary Thermal Management System (TMS), primarily for cooling of the FCS, must be lighter and more compact than the currently available technology [2]. HEXs are essential components of the TMS, as they reject significant quantities of waste heat from the FCS, thereby maintaining the operating temperatures of the LTPEM stack and power electronics. The cooling requirements of an LTPEM FCS-based regional aircraft can result in the need for large, heavy HEXs. Designing these HEXs for compact size is challenging which is necessary for its integration inside small air ducts such as under the aircraft belly or within the propulsion system in the nacelle.

For a regional aircraft powered by an LTPEM FCS and carrying 70 passengers, a total of 5 MW of electric power would be required. An LTPEM FCS with 50% efficiency would release a similar amount of heat as the main by-product, which must be rejected to ensure reliable operation [3]. In a distributed propulsion architecture with ten engines, the heat rejection duty for the TMS in each engine can be estimated at 500 kW and a temperature drop at coolant of 15 K. The HEX is the main component of the TMS and its key function is to cool the hot coolant from the LTPEM by rejecting heat into the ambient air. Another function of the TMS is to precondition the hydrogen fuel by heating it to 353 K prior to entering the LTPEM stack. The size of the main air-cooled HEX can be reduced by transferring some of the heat energy to the fuel preconditioning unit. Details of the propulsion system design, system-level studies and preliminary HEX design work are presented in previous

publications by the author [3] [4] [5].

The key requirements for the TMS and the HEX are to maximize heat transfer while minimizing size and weight. This increases the system-level gravimetric and volumetric power densities, making electric propulsion using an LTPEM FCS a viable solution for aircraft. However, HEX results in pressure loss, which increases the pumping power required for the coolant pumps and air supply unit. Reducing the HEX mass, drag and required pumping power would reduce the associated fuel burn penalties for economic use [6] [7]. This paper examines six HEX designs and calculates their performance for different air inlet conditions. The thermal-hydraulic performance is calculated using a validated CFD method.

2. HEX Designs

Figure 1a illustrates the conceptual design of an LTPEM FCS-based propulsion system and nacelle pod configuration for HEX integration. Figure 1b presents mock-ups of the Gyroid-Pipe and OSF HEX segments.

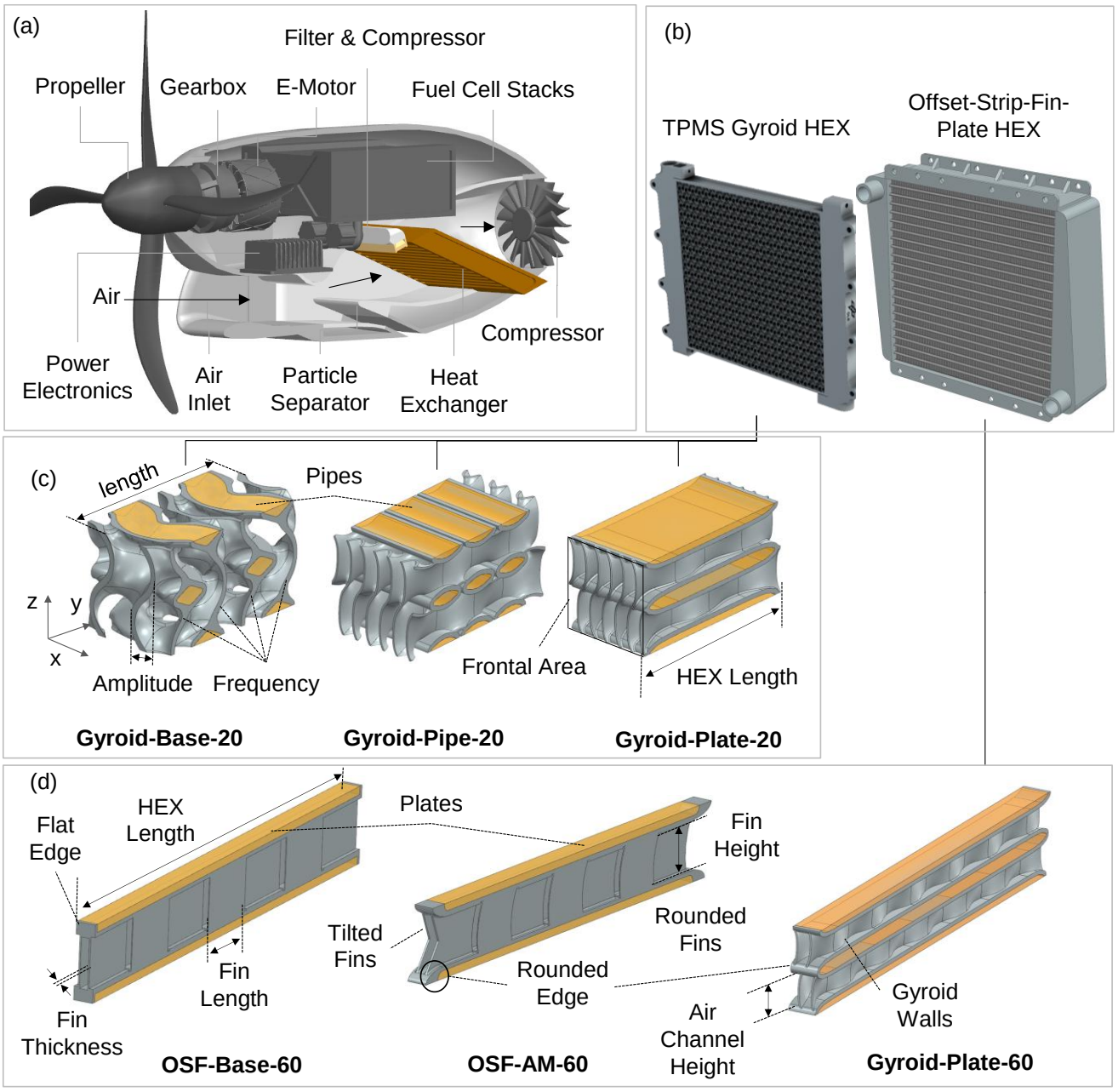


Figure 1 – Conceptual design of a fuel cell powered nacelle integrated propulsion system (a), TPMS based Gyroid HEX and Offset-Fin-Plate HEX mockups (b), designs of HEX unit cells for CFD

assessment (c).

A Gyroid-Base-20 is prototyped using an additive manufacturing process. Experiments measure heat transfer and pressure drop across the air and liquid sides. The test results validate the CFD methodology. Two new TPMS gyroid-based designs are examined. These variants offer higher compactness and differ in coolant channel geometries: Gyroid-Pipe-20 has channels in the form of pipes, and Gyroid-Plate-20 has channels in the form of plates. Both variants have an airside length of 20 mm, similar to the Gyroid-Base-20. Figure 1c shows an illustration of their unit cells. A longer version of Gyroid-Plate-20 is developed by increasing its length threefold and is called Gyroid-Plate-60. Two OSF HEX variants with a 60 mm air side length are included: OSF-AM-60 is designed for additive manufacturing, and OSF-Base-60 is designed as a baseline for conventional manufacturing using a brazing technique. The following section describes the design of the proposed HEXs.

2.1. TPMS gyroid based HEX

Current research into lightweight HEX focuses on polymer composite materials reinforced with thermally conductive fillers. These materials have metal-like heat transfer properties but are significantly lighter [8]. Additive manufacturing is becoming increasingly common in the aviation sector. These innovations and technological advances offer advantages for developing TPMS-based lightweight HEXs. Several different TPMS geometries exist; the sheet gyroid geometry, in particular, provides smooth zero mean curvature, enabling attached flow inside the channels and better mixing of fluids, thereby improving heat rejection. This property is significant for fully developed turbulent flow at high Reynolds numbers. Channeling the flow through triply periodic curvatures increases the turbulent thermal boundary layer along the surface, thereby improving convective heat transfer. However, pressure losses due to additional viscous forces and form drag intensify [9] [10] [11].

The TPMS gyroid structure can be defined using the following implicit equation (1).

$$\begin{aligned} f(x,y,z,l,A_x,A_y,A_z,F_x,F_y,F_z) \\ = A_x sin\left(\frac{2\pi x F_x}{l}\right) cos\left(\frac{2\pi y F_y}{l}\right) + A_y sin\left(\frac{2\pi y F_y}{l}\right) cos\left(\frac{2\pi z F_z}{l}\right) \\ + A_z sin\left(\frac{2\pi z F_z}{l}\right) cos\left(\frac{2\pi x F_x}{l}\right) \end{aligned} \quad (1)$$

It is a trigonometric function of Cartesian coordinates where l is the unit cell length, and the amplitude factors are A_x, A_y, and A_z in each direction. The frequency parameters are F_x, F_y, and F_z, which result in corresponding pitches in each direction. These pitches represent the number of occurrences of curvature. The Gyroid-Base-20 design has uniform amplitudes of A_x = A_y = A_z = 1.25 mm and frequency parameters of 2, resulting in a constant pitch of 5 mm in each direction. In the Gyroid-Pipe-20 and Gyroid-Plate-20 designs, the amplitudes are A_x = 0.6 mm, A_y = 1.25 mm, and A_z = 0.73 mm. The pitch is 1.66 mm in the x-direction and 5 mm in the y- and z-directions. All three gyroid-based designs have a wall thickness of 0.5 mm and unit cell dimensions of 10 mm by 10 mm for the frontal cross-section and a depth of 20 mm along the y-axis airflow direction. In the Gyroid-Base-20, the coolant channels, in form of pipes, are embedded within the gyroid curvatures. The pipes have an oval-shaped cross-section with minor and major radii of 1 and 2 mm, respectively. The coolant channels in the Gyroid-Pipe-20 design are straight pipes with similar cross-sectional geometry. Due to the small amplitudes in the x-direction, the curvature is too small to route the coolant channels along the gyroid walls. Sample prototypes were developed to examine manufacturing quality, and various coolant channel routings were down selected.

The air-wetted surface areas and unit cell volumes are measured using 3D models. The specific surface area, or compactness β, in m²/m³, is calculated as follows:

$$\beta = \frac{A_{air\ wetted}}{Volume_{unit\ cell}} \quad (2)$$

The hydraulic diameter D_h, in m, for the gyroid unit cells can be calculated as ratio of the porosity and the specific surface area as follows:

$$D_h = \frac{4\,\varepsilon}{\beta} \tag{3}$$

where porosity ε is calculated as the ratio of void air volume to the total unit cell volume as:

$$\varepsilon = \frac{Volume_{void\ air}}{Volume_{unit\ cell}} \tag{4}$$

These design properties are listed in Table 1. Due to smaller amplitudes of the gyroid walls along the x-axis, three time more gyroid surfaces are defined in Gyroid-Pipe-20 and Gyroid-Plate-20 relative to the Gyroid-Base-20, causing in smaller values for the D_h. This increases the number of coolant channels and the compactness at the air side. By changing the coolant channel from pipe to plates in Gyroid-Plate-20, the porosity and the compactness reduces, relative to the Gyroid-Pipe-20, as shown in Table 1. All the gyroid-based HEX designs are defined for additive manufacturing using the AlSi10Mg alloy with a density of 2,670 kg/m³ [12]. Table 1 shows the key design properties for the HEX unit cells.

Table 1 – Key design properties of HEX unit cells.

		Gyroid-Base-20	Gyroid-Pipe-20	Gyroid-Plate-20	Gyroid-Plate-60	OSF-AM-60	OSF-Base-60
Compactness β	m^2/m^3	642	1237	1078	987	1132	1249
Porosity ε	%	62.3	65.7	47.8	45.6	57.1	55.4
D_h	mm	3.88	2.12	1.77	1.77	1.75	1.75
Fin / Gyroid pitch	mm	5	1.66	1.66	1.66	1.2	1.2
Fin / Gyroid height	mm	2.53	2.53	2.53	2.53	6.35	6.35

2.2. OSF

Through the preliminary design work, done in [13], an optimized OSF geometry was identified and modified with an air channel length of 60 mm, denoted as OSF-Base-60. Design optimization was performed for high performance, low mass, and low pressure loss using experimentally defined correlations. This resulted design has flat fin edges and blunt edges for the coolant plates, as indicated in Figure 1d. With a fin thickness of 0.1 mm, a fin length of 8.49 mm, a fin height of 6.35 mm, and a 0.5 mm gap between each offset pair along its length; a compactness is calculated as β = 1249 and porosity as ε = 55.4%. This optimized geometry is improvised geometry over 1/8-15.61 kays & London geometry [13].

Of all the considered HEX designs, the OSF-Base-60 is the most compact, resulting in the least D_h of 1.75 mm. Table 1 lists the key design attributes. This design is intended for a conventional manufacturing technique that uses sheet metal and brazing. It serves as the baseline design for plate HEXs with 60 mm air channel lengths. To study flow characteristics and improve hydraulic performance, a modified version, OSF-AM-60, was developed, as shown in Figure 1d. Using additive manufacturing to create a fin thickness smaller than 0.2 mm is challenging because it reduces surface quality and stiffness. Several unit cell probes were 3D printed, and after a structural inspection, the design parameters for the best quality were determined. The leading and trailing edges of the coolant plates are now aerodynamically oval-shaped, with major and minor radii of 4 mm and 1 mm, respectively. This results in a thickness of 3 mm, which provides additional structural stiffness in the event of a collision with debris. The front row of fins is slanted at 57° to enable additive manufacturing and increase the stiffness of the coolant plates. The rest of the fin edges are rounded with an 8 mm radius, and a 0.5 mm gap is defined between the fin rows to optimize 3D printing in the y-direction. The coolant plates are 0.5 mm thick with a 2 mm channel height. The frontal area of

the unit cell is 2.4 mm x 9.35 mm, and its effective length for the air channel 60 mm and 70.43 mm including the oval-shaped edges. D_h is calculated as the ratio of the free flow cross section between a pair of fins to the perimeter of the 3D model.

3. Performance Evaluation Methodology

For performance calculations, CFD simulations use small unit cells for each HEX type, as illustrated in Figure 1c. Figure 2b shows an example of CFD domains with a Gyroid-Base-20 unit cell, consisting of air, solid and coolant domains. The goal is to perform a conjugate heat transfer simulation by calculating the conduction and convection of heat from the hot coolant stream through the solid unit cell body into the cold air stream. The domains are aligned in a cross-flow HEX configuration with mass flow inlet conditions assigned to the air and coolant inlet faces. A gauge pressure of 1 bar is applied to all inlets and outlet boundaries. At the remaining outer boundaries, a periodic symmetry condition is applied. A coupled thermal condition and a wall roughness of 10 µm are applied to the wall surfaces of the solid domain. This roughness value is typical for an additive manufactured surface made of AlSi10Mg [12].

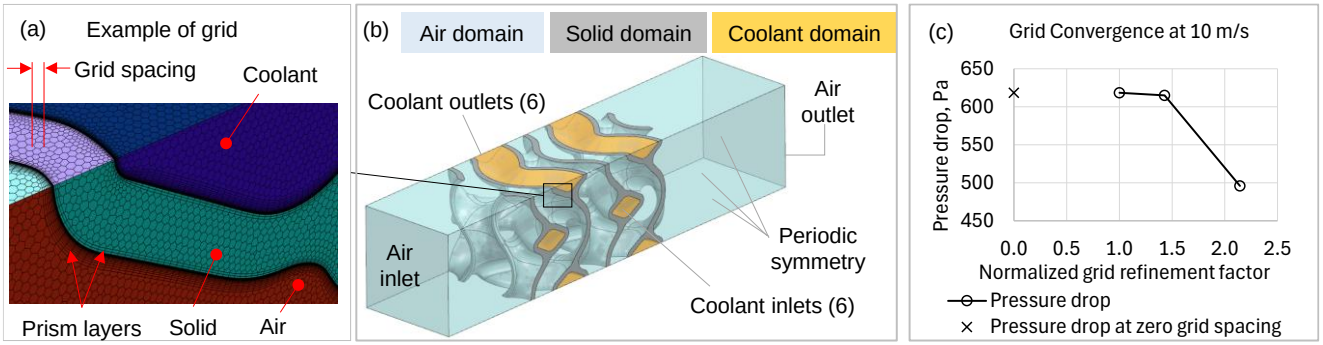


Figure 2 – Example of CFD grid (a), geometry of CFD domain (b) and grid convergence result (c).

Table 2 – Key material properties for air, water and solid material.

		Unit	Air [14]	Water	AlSi10Mg [12]
Density	ρ	kg/m^3	Ideal gas model	998.2	2670
Thermal conductivity	k	W/(m K)	$f\ (T_{air})$	0.6	173
Specific heat capacity	C_p	J/(kg K)	$f\ (T_{air})$	4182	890

Furthermore, material properties for the air, solid and water as coolant are applied in terms of density ρ, thermal conductivity k and specific heat capacity C_p as per the Table 2. For the CFD assessment ANSYS Fluent 2024 R1 [14] is used and temperature dependent piecewise linear correlations from the Fluent database [14] are applied for the thermal conductivity k and specific heat capacity C_p of the air. The thermal-hydraulic performance is quantified using the key definitions, generally explained in reference [9] and modified for compact TPMS structures in [15] [16]. For the thermal performance, the Heat Transfer Rate (*HTR*), in W, is calculated as a product of mass flow rate $\dot{m}$, the specific heat capacity $C_{p,}$ and the temperature difference along a fluid stream. For the *HTR* calculation, mass-weighted average is calculated for the temperature difference at the air inlet and outlet:

$$HTR = \dot{m}_{air}\, C_{p\,air}(T_{inlet\ air} - T_{outlet\ air}) \tag{5}$$

The Heat Transfer Coefficient (*HTC*), in W/m^{2}K, defines the amount of heat transfer per unit surface area and per unit temperature change between the surface and fluid. *HTC* is calculated using the heat flux q, and the temperature difference as:

$$HTC = \frac{q}{(T_{wall} - T_{bulk})} \quad (6)$$

The heat flux *q* and wall temperature T_{wall} are calculated from CFD results as surface average on the air-wetted walls and the bulk temperature T_{bulk} of the air results from the volume weighted average.

Along the air and coolant domains, total pressure drops due to viscous and form drag inside their respective channels. This also includes the entry and exit effects, caused by the shape of the coolant plates at leading and trailing edges. Typically, a pump or compressor is used to overcome this pressure drop and to maintain the required mass flow rates.

For the hydraulic performance, the pumping power (*PP*), in W, is calculated as a product of ΔP_{tot} across the fluid domain and the volume flow rate as a ratio of the mass flow rate $\dot{m}$ and density ρ as:

$$PP = \frac{\Delta P_{tot}\, \dot{m}}{\rho} \quad (7)$$

In this work, only the air side *PP* is considered as the coolant has small mass flow rates and its pressure drop is significantly lower than that at the air side. Accurate calculation of ΔP_{tot} is essential for sizing the air supply systems and specially for the compressor design.

The combined thermal-hydraulic performance is calculated using the so-called Power Ratio (*PR*) as ratio of the *HTR* to the *PP*.

$$PR = \frac{HTR}{PP} \quad (8)$$

PR shows how well a HEX performs in terms of heat rejection compared to *PP* consumption. *PP* is weighed against the aircraft-level fuel burn penalty. The higher the *PP* for the HEX, the higher the fuel consumption due to the electric power required for the compressor and its mass. According to the Thermal Management Roadmaps [2], HEX for fuel cell cooling should deliver a *PR* > 5, which means, *HTR* should be at least five times higher than its *PP*.

The drag produced by the HEX is calculated using the surface integral of the pressure and viscous forces acting on the air-wetted walls. This entity is used in overall penalty estimation together with *HTR* and *PP*. The Cost Function (*CF*) is defined to minimize *PP* and drag force while maximizing power density (*PD*) as ratio of *HTR* to the total mass. In this study, all six HEX designs are compared and *CF* is calculated for full size HEX for 500 kW of heat duty at its design point with air inlet velocity of 20 m/s. For the *CF*, normalized values of *PD, PP* and drag are implemented, as well as an equal weighting factor among them.

$$CF = PD_{norm} - PP_{norm} - Drag_{norm} \quad (9)$$

The normalized values of these three variables are calculated by dividing the difference between the nominal and minimum values by the difference between the maximum and minimum values. *CF* shows the net improvement in *PD*s at TMS level, after the *PP* and drag penalties have been subtracted.

3.1. Grid convergence

The grid generation, simulation and post-processing for the CFD assessment are carried out using ANSYS Fluent 2024 R1 software [14]. The surface mesh is generated using mesh refinement factors for thin edges and curvatures. The maximum face size is set as a control parameter for conducting a grid convergence study. For the volume mesh, 20 prism layers are assigned to the surfaces wetted by air in the air domain, and 10 layers are assigned to the surfaces wetted by coolant in the coolant domain. The final mesh is converted into polyhedral elements to ensure smooth transitions and mesh

orthogonality above 0.2 and element skewness below 0.8. Figure 2a shows an example of the mesh, with detailed views of the prism layers and grid spacing. CFD simulations are performed using a 3D, pressure-based, transient solver with double precision. Temperature properties are assigned to enable conjugate heat transfer across the CFD domains.

To examine the spatial convergence of a CFD simulation, a grid sensitivity study is performed in accordance with reference [17]. This study includes the determination of ordered discretization error and dependency on grid refinement. Three meshes with grid spacings of 0.07 mm, 0.1 mm and 0.15 mm were generated, resulting in a normalized grid spacing factor of 1, 1.43 and 2.14, and a number of mesh elements of 12.7 million, 6.6 million and 5.1 million, respectively. CFD simulations were carried out using the KW-SST turbulence model with an air inlet velocity of 10 m/s, and the pressure drop between the air inlet and outlet was measured. For a detailed understanding of the grid convergence study and the parameters utilized, refer to the CFD Verification and Validation practice in [17]. The key results are summarized in Table 3 and the grid sensitivity plot is presented in Figure 2c.

Table 3 CFD grid data and results from grid convergence study for air inlet velocity of 10 m/s.

Grid ID		1	2	3
Grid face size	mm	0.07	0.1	0.15
Number of elements	-	12719681	6631505	5171270
Normalized grid spacing	-	1	1.43	2.14
Pressure drop, ΔP	Pa	ΔP_1 = 618.5	ΔP_2 = 615.1	ΔP_3 = 495.8
Order of convergence (*OC*)	-	5.152		
Pressure drop at zero grid spacing	Pa	618.6		
Grid convergence index *GCI*-12	%	0.019		
Grid convergence index *GCI*-23	%	0.701		
Asymptotic range of convergence	-	1.005		

The order of convergence (*OC*), assuming second order numeric is calculated as [17]:

$$OC = ln\left[\frac{\Delta P_3 - \Delta P_2}{\Delta P_2 - \Delta P_1}\right] / ln\,(2) \tag{10}$$

where the pressure drop values are denoted as ΔP_1, ΔP_2 and ΔP_3 with Grid 1, Grid 2 and Grid 3 respectively in their decreasing order of grid refinement. *OC* of 5.152 is calculated for air inlet velocity of 10 m/s. The calculated *OC* is higher than the theoretical value of 2, which is most likely due to grid stretching, quality and non-linearities in solution and compressibility effects. Values for the ΔP are extrapolated for very fine grid resolution at zero grid spacing using Richardson method [17].

$$\Delta P_{zero\ grid\ spacing} = \Delta P_1 + \frac{(\Delta P_1 - \Delta P_2)}{(2^{OC} - 1)} \tag{11}$$

In Figure 2c, values of the ΔP from the CFD simulations at 10 m/s with all three grids are plotted together with the extrapolated values at zero grid spacing over the normalized grid refinement factor. Notable differences can be seen between the values from Grid 2 and Grid 3. At an air inlet velocity of 10 m/s, the ΔP is underestimated with the coarse mesh. With the medium-resolution grid, the results match those of the fine grid, and the error margin is small compared to the extrapolated values at zero grid spacing. The grid convergence index (*GCI*) is calculated to quantify convergence and the error band.

The grid convergence index, *GCI,* for the fine grid solution can be calculated using a safety factor of 1.25, as three grids are used to estimate the *OC*, according to the reference [17]:

$$GCI_{12}(\%) = \frac{1.25\ abs\left|\frac{\Delta P_{tot\ 1} - \Delta P_{tot\ 2}}{\Delta P_{tot\ 1}}\right|}{(2^{OC} - 1)}\ 100 \tag{12}$$

$$GCI_{23}(\%) = \frac{1.25\ abs\left|\frac{\Delta P_{tot\ 2} - \Delta P_{tot\ 3}}{\Delta P_{tot\ 2}}\right|}{(2^{OC} - 1)}\ 100 \tag{13}$$

To check if the solutions are within the asymptotic range of convergence, the ratio $GCI_{23}/(2^{OC}\ GCI_{12})$ is calculated. The value *GCI* of is close to one, indicating that the solution is within the asymptotic range of convergence. Based on the grid convergence study, the estimated ΔP at 10 m/s is 618.6 Pa, which can be achieved with a medium-resolution grid 2, with an error band of 0.019 Pa (1.9%) Based on these results, a medium-resolution grid with a face size of 0.1 mm, 20 prism layers in the air fluid domain, and at least 10 layers in the coolant domain is selected. These grid settings are applied to all HEX unit cells for the CFD simulations.

3.2. Turbulence model validation

Another study is required to validate the selection of the CFD turbulence model against experimental data, due to the uncertainty of the turbulence model. The author conducted and published the experimental work in previous studies [18] and [19]. The following section provides a brief summary of the experimental work used to validate the CFD model and setup.

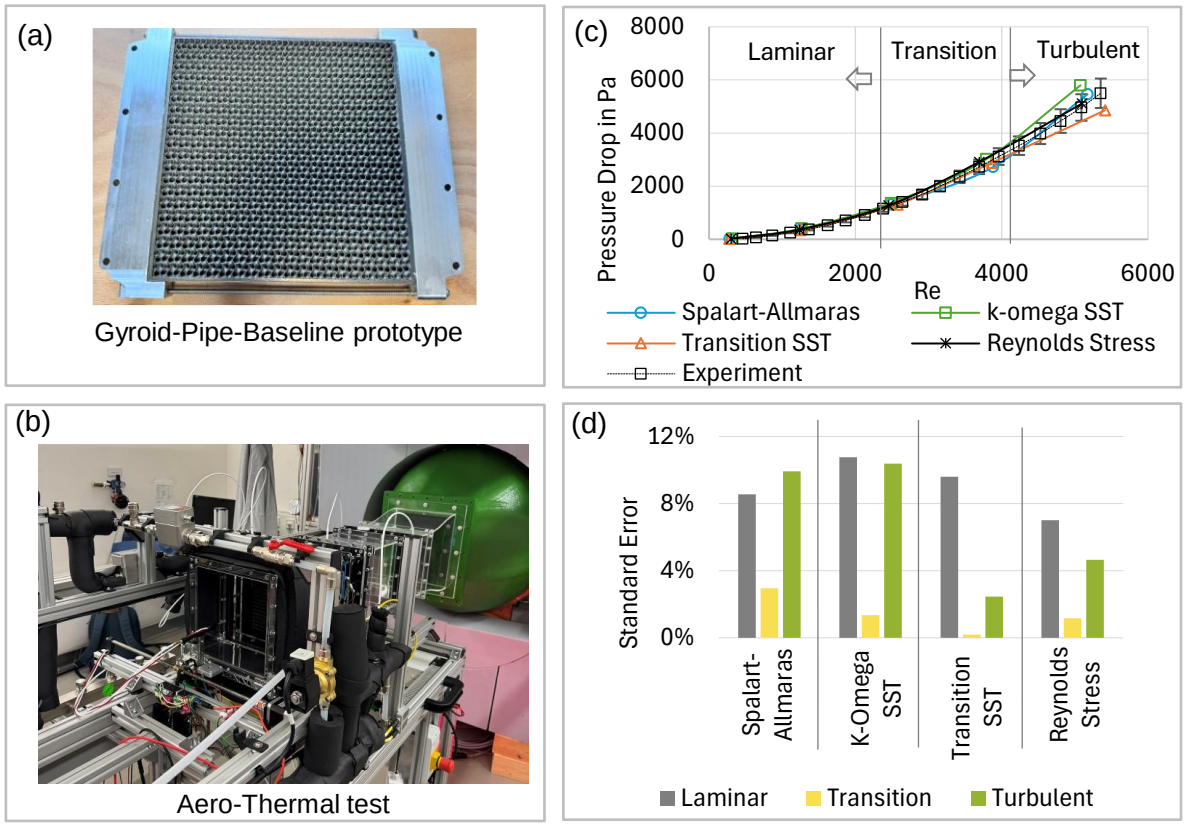


Figure 3 – Prototype of Gyroid-Base-20 for aero-thermal test (a), test rig setup (b), pressure drop across the air side using different CFD turbulence models and experimental data (c) and standard error in pressure drop relative to test data (d).

The prototype for the experiment was developed using 400 Gyroid-Base-20 unit cells (shown in Figure 1c), arranged sequentially inside a 200 mm x 200 mm x 20 mm volume to form the core (Figure 3a). This configuration results in 39 pairs of coolant channels arranged in a cross-flow pattern

and connected to the coolant bulkheads. The manufacturing process involves using a powder of the AlSi10Mg alloy on a 3D metal printer with a selective laser melting process [12]. Experiments are conducted on the DLR Institute of Electrified Aero Engines Thermal Management Testrig Modular Air Duct (TMTmad) [20], as shown in operation in Figure 3b. The static pressure drop across the air side of the HEX is measured using a differential pressure sensor capable of measuring a monodirectional range of 7.5 kPa with an accuracy of ±0.01875 kPa. Air pressure tubes are connected to four small holes drilled in the center of the duct's side walls, 2 cm from the HEX inlet and outlet planes. Experiments are run for air inlet velocities of up to 25 m/s.

ANSYS Fluent offers a variety of turbulence models for solving the energy and mass transport equations. In this study, four turbulence models were selected to validate the CFD setup. These are: the Spalart-Allmaras one-equation model [21]; the k-ω SST model [22], which has two additional transport equations for turbulence shear stress; the Transition SST model [23], which is a four-equation model; and the Reynolds Stress model, which has seven equations to resolve Reynolds shear stresses in each flow direction. Further details on their parameters can be found in the ANSYS Fluent user guide and theory manual [14].

The pressure drop along the air side and across the HEX is calculated using the aforementioned turbulence models, and the results are compared with the experimental data. The pressure drop values are plotted against the air flow Reynolds number in Figure 3c. A 10% margin band has been added to illustrate the normalized values relative to the test data more clearly. The flow remains laminar ($Re < 2300$) for air inlet velocities below 9.5 m/s and turbulent ($Re > 4100$) for velocities above 17 m/s. A slight difference in Re numbers can be seen, especially in the fully turbulent region, indicating a variation in the average bulk velocity inside the Gyroid-Base-20 air domain when different turbulence models are used. For a quantitative assessment, the percentage change in the standard deviation error relative to the test data is calculated and plotted in Figure 3d for each turbulence model. The figures are colored according to the laminar, transition and turbulent zones.

In the laminar region, the Reynolds Stress model provides the best prediction, followed by the Spalart-Allmaras, Transition SST and k-ω SST models, which have relative standard error changes of 7%, 8.5%, 9.6% and 10%, respectively. With all turbulence models, the pressure drop is underpredicted at lower velocities and overpredicted in the higher laminar flow region. Within the transition zone ($2300 < Re < 4100$), all turbulence models overpredicted the pressure drop values relative to the test data.

The Transition SST model provides the best approximation, followed by the Reynolds Stress, k-ω SST and Spalart-Allmaras models, with standard errors of 0.2%, 1.2%, 1.4% and 3%, respectively. Similarly, in the fully turbulent region, the average deviation for the Transition SST, Reynolds Stress, Spalart-Allmaras and k-ω SST models is 2.5%, 4.6%, 9.9% and 10.4% respectively. According to theories referred to in [23] and [17], the Transition SST model is valid for the transition between laminar and turbulent flow and fully developed turbulent flow. It is also suitable for wall-bounded flows with no free shear flows. The Transition SST model provides the best approximation in the transition and turbulent regions, which constitute the general operating range for the HEX and are used for the CFD assessment in this work.

The boundary conditions for the CFD assessment are defined from the 500 kW cooling requirement for the TMS of a LTPEM FCS. HEX has to deliver a 15 K temperature drop at the coolant loop, with a constant velocity of 1 m/s inside the channels. On the air side, five CFD cases are run with inlet velocities of 1.13, 5, 10, 15 and 20 m/s, each with an air inlet temperature of 297.35 K. A gauge pressure of 101325 Pa was defined at all inlet and outlet planes. For the AoA assessment with tilted HEX, CFD simulations are performed for air inlet velocity of 20 m/s and AoA of 9°, 18°, 27°, 36° and 45° relative to the frontal area normal. The convergence criteria for the continuity equations, velocities in each direction, energy and turbulence entities are set to a minimum residual limit of 10^{-4}. Additionally, the mass flow rate, temperature and total pressure are monitored at the inlets and outlets to study solution convergence. The CFD case is initialized using air inlet boundary conditions. Additionally, a full multi-grid initialization is performed. The following section presents the performance results for all four HEX unit cells, obtained using the validated Transition SST

turbulence model and grid settings.

4. Result

This section deals with the performance characterization of HEX unit cells using CFD results. To study the thermal and hydraulic performance, a comparison is made between all six HEX designs and their respective baseline designs for 20 mm and 60 mm. Scaling the unit cell thermal and hydraulic results estimate the HEX sizing for 500 kW LTPEM FCS cooling at a design performance point of 20 m/s air inlet velocity. A sensitivity study of AoA from 0° to 45° is performed at the same operating point, and a comparative assessment is made to the best-fit design for potential nacelle and aircraft belly pod integration.

4.1. Performance characterization using unit cell designs

The *HTC* and the total pressure drop across the HEX air side are used to characterize the thermal-hydraulic performance of the HEX. Figure 4 plots the respective values of each of the six HEX unit cell designs against the air inlet velocity.

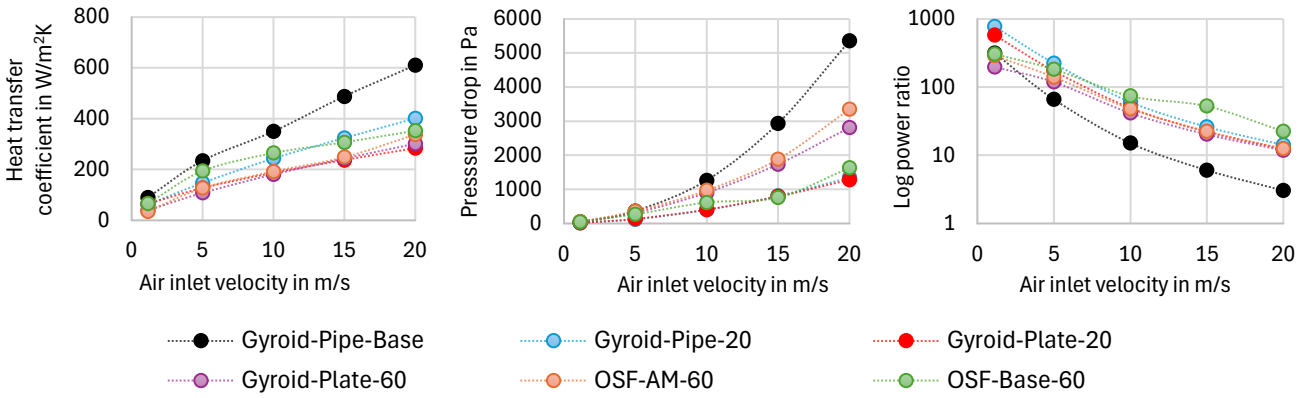


Figure 4 – Performance results from unit cell CFD assessment.

Gyroid-Base-20 has the highest *HTC* values and thermal performance, but the HEX air side has a high pressure drop. For *PR* > 5, the operating point for Gyroid-Base-20 should be under 15 m/s of air inlet velocity. Gyroid-Pipe-20 is the second highest *HTC* for velocities above 15 m/s, delivering 75% less pressure drop and 4.3-times higher *PR* than Gyroid-Base-20. This design is the second best after OSF-Base-60. Modifying the coolant pipes into plates, Gyroid-Plate-20, improves hydraulic performance with 10% less pressure drop but has 30% lower *HTC* values. Increasing the air channel lengths from 20 mm to 60 mm, Gyroid-Plate-60 improves the *HTC* further by 6.4% for operating points above 15 m/s, but has 2.5 times higher pressure loss than Gyroid-Plate-20. Gyroid-Plate-60 has double the coolant channels and half the air channel height of OSF-Base-60, as shown in Figure 1d. With Gyroid-Plate-60, there is no performance gain relative to OSF-Base-60 as the air side pressure drop increases by an average of 1.8 times and the *HTC* drop by 12% for air velocities above 10 m/s. A comparison between OSF-AM-60 and OSF-Base-60 shows that increasing the fin thickness from 0.1 to 0.2 mm and modifying the fin and plate edges increases the blockage ratio for the free flow inlet area and calculates a 1.7 times higher pressure loss with OSF-AM-60. The same is true for the thermal performance, as the HTC values of OSF-AM-60 are, in average, 20% lower than those of OSF-Base-60. OSF-Base-60 delivers the highest combined performance values for *PR* at operating points with air velocities of > 10 m/s, and Gyroid-Pipe-20 delivers the highest performance at lower air velocities, as plotted in Figure 4.

4.2. HEX sizing for design point

The design operating point for HEX sizing and TMS is selected at an air inlet velocity of 20 m/s in the take-off condition. The HEX size is calculated for a total heat duty of 500 kW for LTPEM FCS cooling. The width of the HEX is calculated by multiplying the number of required unit cells, calculated by dividing the required 15 K temperature drop at the coolant side through the temperature drop

across each unit cell. The HEX height is defined by summing the *HTRs* across the HEX width and the number of individual widths, totaling 500 kW. HEX mass is calculated using the total number of unit cells. The fan mass is linked to the *PP* and is calculated using correlations as referenced in [24]. Gravimetric power density is calculated for 500 kW cooling requirement at HEX and TMS level, where the fan mass is included. The normalized cost function is defined as per the Equation (9), which is normalized by the OSF-Base-60 as the highest positive performance outcome after deducting the *PP* penalties and drag. Table 4 shows the performance and size results.

Table 4 HEX performance and size results for 500 kW heat duty.

		Gyroid-Base-20	Gyroid-Pipe-20	Gyroid-Plate-20	Gyroid-Plate-60	OSF-AM-60	OSF-Base-60
Pumping power	kW	197	42	53	49	46	27
HTC	W/m^{2}K	610	402	284	302	338	387
PR	-	3	12	9	10	11	18.4
Air flow rate	kg/s	36.9	31.6	42.3	17.3	13.9	15.2
Coolant flow rate	kg/s	7.51	7.84	8.03	7.57	7.92	7.79
HEX width	m	0.37	0.35	1.09	1.56	0.98	1.04
HEX height	m	4.03	3.79	1.60	0.45	0.58	0.61
HEX length	m	0.02	0.02	0.02	0.06	0.07	0.06
Frontal area	m^2	1.48	1.31	1.76	0.71	0.57	0.64
HEX mass	kg	24.4	19.5	34.0	41.2	32.5	18.5
Fan mass	kg	158.4	135.9	180.9	75.6	61.4	67
PD HEX	kW/kg	20.5	25.7	14.7	12.1	15.4	26.9
PD TMS	kW/kg	2.7	3.2	2.3	4.3	5.3	5.8
Normalized cost function	-	-1.88	0.02	-0.35	0.24	0.56	1

The investigation of HEX unit cells shows that TMS cannot be sized from unit cell thermal-hydraulic performance alone. Scaling to the required 500 kW heat duty reveals the importance of system-level metrics like frontal area, air mass flow rate, fan mass, pressure loss, gravimetric power density, and installation envelope. Gyroid-based concepts are attractive at the unit-cell level due to their three-dimensional channel topology, which promotes flow mixing and convective heat transfer (see Table 4 and Figure 4). However, their short air-side flow length of ~20 mm leads to a large frontal area after scaling, increasing the total air mass flow rate and, thus, the required fan size and mass. Consequently, the local thermal advantage of the gyroid unit cell does not directly translate into an aircraft-level heat-exchanger design under the current scaling assumptions.

A key limitation of gyroid concepts is their sensitivity to flow-length scaling. While increasing the flow length from 20 mm to 60 mm or more could reduce the frontal area requirement and improve integration in narrow air ducts but, it would also increase airside pressure drop and fan power due to the longer flow path and sustained frictional losses within the complex internal topology. As shown in Table 4, Gyroid-Plate-60 requires 2.5 and 3.5 times less frontal area and HEX height, respectively, than Gyroid-Plate-20.

In contrast, OSF-based concepts offer a better balance at the system level between thermal-hydraulic performance, flow length, pressure drop, frontal area, and installation volume. The OSF-Base-60 and OSF-AM-60 configurations satisfy the one meter nacelle-width constraint while maintaining a practical core aspect ratio and avoiding the excessive frontal-area growth observed in gyroid concepts. The *PR* remains similar among the investigated geometries because the heat duty is fixed at 500 kW. For nacelle-integrated PEMFC TMS, more discriminating metrics include combined HEX and fan mass, air mass flow requirement, pressure-loss penalty, installation envelope, and gravimetric power density.

4.3. Effect of AoA

Table 4 shows that HEX over one meter tall can only be integrated inside a nacelle at a tilted position.

The AoA for the airflow at the HEX's frontal area increases. This section examines the effect of increasing AoA for a constant mass flow rate calculated for an air inlet velocity of 20 m/s. Results are presented in terms of normalized *HTC, PP*, and drag force (see Figure *5*). The figures show the effect of different AoAs (0°, 9°, 18°, 27°, 36°, and 45°). Figure *6* shows an example of wall shear stress, wall temperature, and velocity path lines for an AoA of 36°. It also shows detailed views of flow separations at the HEX leading and trailing edges.

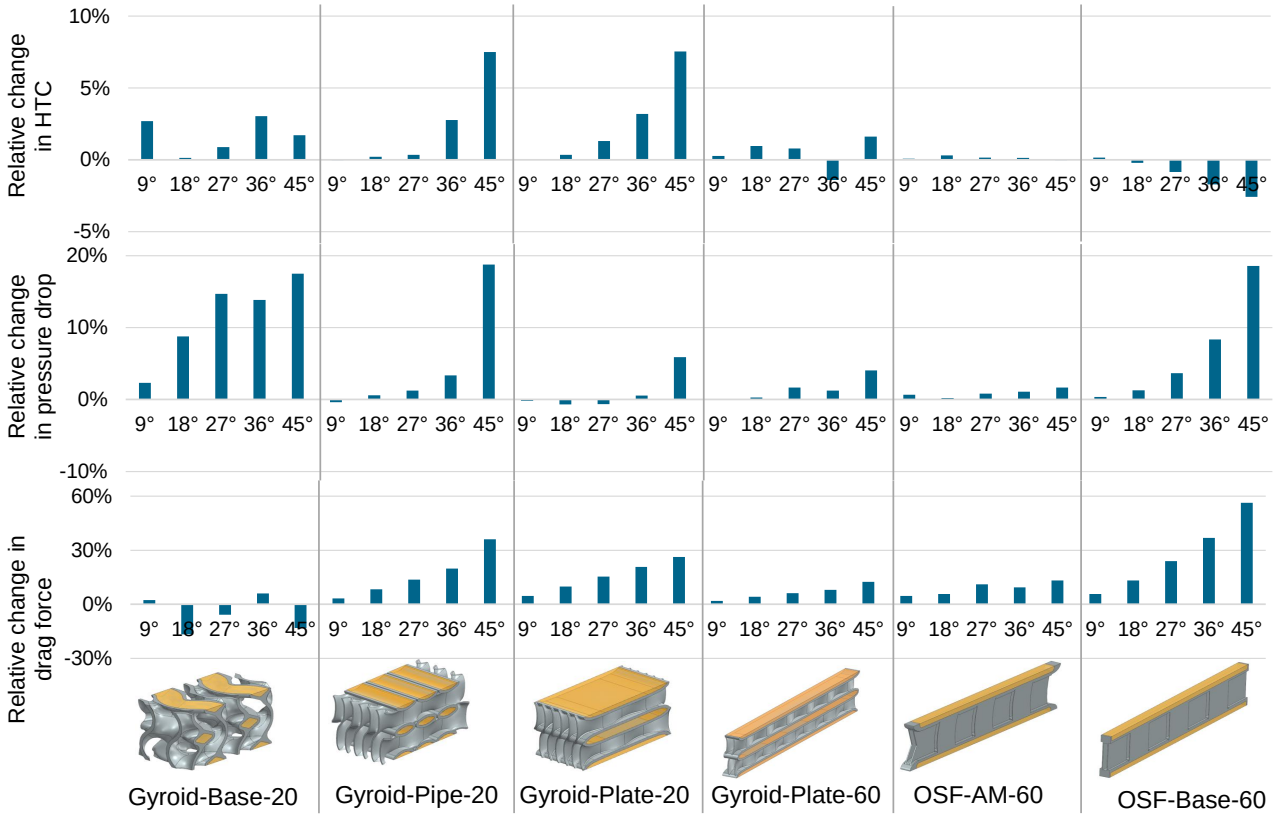


Figure 5 – Relative change in heat transfer coefficient, drag and pumping power with increasing angles of attack.

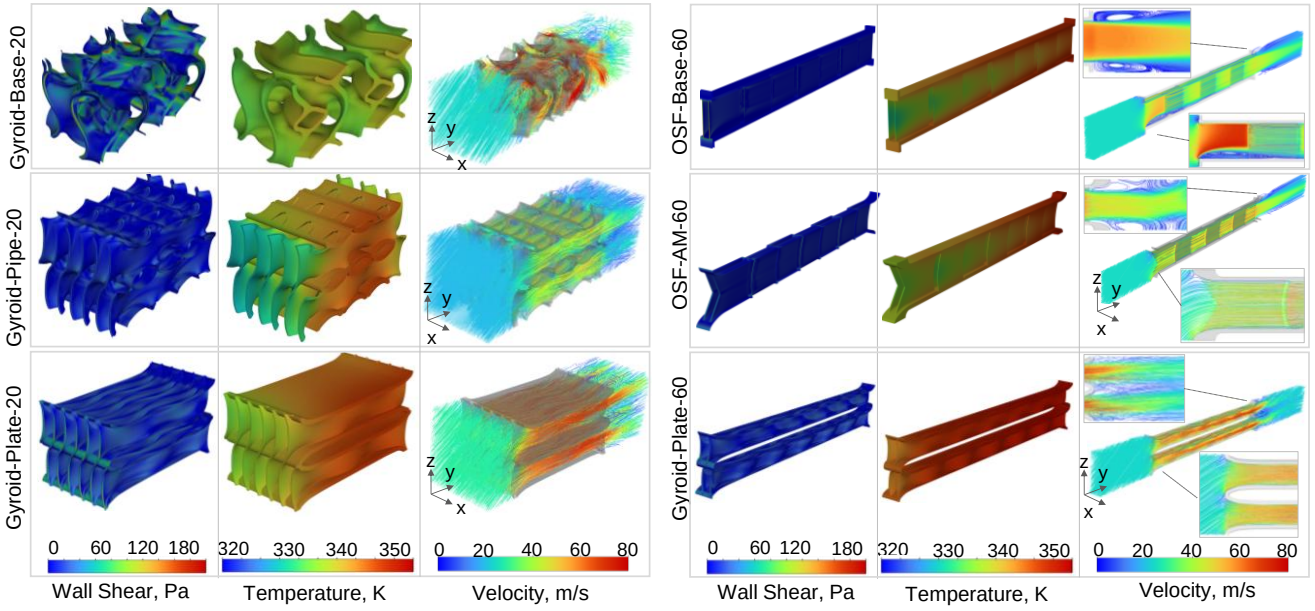


Figure 6 – Wall shear, temperature and velocity plots 36° angle of attack.

As AoA increases, flow and turbulence in the non-axial directions also increase. Depending on the

gyroid curvature and flow dynamics, convective heat transfer increases due to additional turbulence in the non-axial direction. Gyroid-Base-20 experiences the highest pressure loss. Its large gaps between the gyroid walls and coolant channels cause wall shear to increase with higher velocity components in the non-axial direction (see Figure *6*). The Gyroid-Pipe-20 and Gyroid-Plate-20 designs share the same TPMS structures and D_h. An increment in *HTC* is observed at AoA above 27° for both designs. The same is true for the drag increment, as viscous forces dominate due to non-axial flow. The pressure drop increases dramatically at AoA of 45° with Gyroid-Pipe-20. In contrast, Gyroid-Plate-20 is very insensitive to pressure drop as the flow remains contained between the flat coolant plates.

The OSF-AM-60 shows little to no change in thermal performance and pressure drop against AoA. Despite having twice the fin thickness, OSF-AM-60's modified fins and aerodynamically shaped plate edges show lower drag and pressure drop. The OSF-Base-60's blunt flat edge causes large regions of reverse flow at the inlet and wake, as shown in Figure *6*. This HEX design loses thermal and hydraulic performance at higher AoAs, reaching up to 2.6% *HTC* reduction, 18.6% pressure drop, and 56% drag increment relative to AoA of 0°.

5. Conclusion

The OSF-Base-60 remains a robust reference due to its plate-fin topology, balanced compactness, and practical manufacturability. It has high thermal-hydraulic performance and requires less pumping power, making it suitable for passive cooling without a compressor. It can be integrated underneath the aircraft bally without tilting. This concept is suitable for Megawatt-Level cooling requirements and can be manufactured using aviation-certified manufacturing processes.

Gyroid HEXs have local performance benefits, but their penalties must be evaluated with aircraft-level penalties. The Gyroid-Pipe-20 design is the best performing HEX design, with 20 mm thickness, in terms of combined thermal-hydraulic performance and has the least cost penalty. It is ideal for inclined integration at an angle of up to 27°, but above that, the pumping power penalty becomes dominant.

Taking into account the system-level effects, the OSF-AM-60 design offers the most favorable compromise among the examined concepts. Its advantages arise from its thermal-hydraulic performance and the combined balance of realistic flow length, nacelle width compatibility, limited fan mass penalty, and favorable gravimetric power density. With a width under 1 m and a height of 0.6 m, 500 kW of cooling can be realized with the OSF-AM-60 at a moderate penalty against mass and pumping power. Its low sensitivity to increasing AoA makes this concept suitable for integration in narrow domains with a tilted position.

6. Future work

Future work includes testing and validating the OSF-Base-60 design. A 200 mm x 200 mm x 60 mm prototype is being developed for this purpose. The OSF-AM-60 design is being optimized, including fin grading along the flow direction and modifications for additive manufacturing. A similar prototype will be developed, and experiments will be conducted soon.

7. Contact Author Email Address

The corresponding author email address for further contact is chetan.sain@dlr.de

8. Copyright Statement

The authors confirm that they, and/or their company or organization, hold copyright on all of the original material included in this paper. The authors also confirm that they have obtained permission, from the copyright holder of any third-party material included in this paper, to publish it as part of their paper. The authors confirm that they give permission, or have obtained permission from the copyright holder of this paper, for the publication and distribution of this paper as part of the ICAS proceedings or as individual off-prints from the proceedings.

References

[1] Air Transport Action Group, “Waypoint2050,” [online], Sep 2020, www.atag.org.

[2] Webber, H., Llambrich, J., and Davoudi, H., “Thermal Management Roadmap Report,” https://www.ati.org.uk/wp-content/uploads/2022/03/FZO-PPN-COM-0019-Thermal-Management-Roadmap-Report.pdf.
[3] Sain, C. K., Hänsel, J., and Kazula, S., “Conceptual Design of Air and Thermal Management in a Nacelle-Integrated Fuel Cell System for an Electric Regional Aircraft,” *AIAA AVIATION 2023 Forum,* American Institute of Aeronautics and Astronautics, Reston, Virginia, 2023.
[4] Sain, C. K., Kazula, S., and Enghardt, L., “ELECTRIC PROPULSION FOR REGIONAL AIRCRAFT-CRITICAL COMPONENTS AND CHALLENGES,” *Deutscher Luft- und Raumfahrtkongress (DLRK) 2022* [online], https://elib.dlr.de/193343/.
[5] Sain, C. K., Hänsel, J., and Kazula, S., “Preliminary Design of Air and Thermal Management of a Nacelle-Integrated Fuel Cell System for an Electric Regional Aircraft,” *2023 IEEE Transportation Electrification Conference & Expo (ITEC),* IEEE, 2023, pp. 1–8.
[6] Kozulovic, D., “Heat Release of Fuel Cell Powered Aircraft,” GPPS, 2020.
[7] Drela, M., “Aerodynamics of heat exchangers for high-altitude aircraft,” *Journal of Aircraft*; Vol. 33, No. 1, 1996, pp. 176–184. doi: 10.2514/3.46919.
[8] Fraunhofer IFAM, “Process technology for filament production for 3D printing,” https://www.ifam.fraunhofer.de/en/technologies/filament-production-for-3D-printing.html, [retrieved 2025].
[9] Kays, W. M., and London, A. L., “Compact Heat Exchangers,” 2018.
[10] Al-Ketan, O., Ali, M., Khalil, M., Rowshan, R., Khan, K. A., and Abu Al-Rub, R. K., “Forced Convection Computational Fluid Dynamics Analysis of Architected and Three-Dimensional Printable Heat Sinks Based on Triply Periodic Minimal Surfaces,” *Journal of Thermal Science and Engineering Applications*; Vol. 13, No. 2, 2021. doi: 10.1115/1.4047385.
[11] Yu, X., Moreira, T. A., Chen, B., Rankouhi, B., Thoma, D. J., Anderson, M. H., and Qian, X., “Data-driven optimization, additive manufacturing and thermohydraulic testing of a high-temperature Gyroid-based TPMS heat exchanger,” *Applied Thermal Engineering*; Vol. 280, 2025, p. 128422. doi: 10.1016/j.applthermaleng.2025.128422.
[12] EOS GmbH, “EOS Aluminium AlSi10Mg Material Data Sheet,” https://www.eos.info/de/var/assets/03_system-related-assets/material-related-contents/metal-materials-and-examples/metal-material-datasheet/aluminium/material_datasheet_eos_aluminium-alsi10mg_en_web.pdf.
[13] Bhapkar, S., Sain, C., and Kazula, S., “Design of Heat Exchangers with Cooling Fins in Fuel Cell-Powered Electric Aircraft: Genetic Optimization Approach with CFD Validation,” *2025 IEEE/AIAA Transportation Electrification Conference and Electric Aircraft Technologies Symposium (ITEC+EATS),* IEEE, 2025, pp. 1–8.
[14] *ANSYS Fluent. User Guide*, ANSYS. Inc. Release 2024 R1.
[15] Reynolds, B. W., Fee, C. J., Morison, K. R., and Holland, D. J., “Characterisation of Heat Transfer within 3D Printed TPMS Heat Exchangers,” *International Journal of Heat and Mass Transfer*; Vol. 212, 2023, p. 124264. doi: 10.1016/j.ijheatmasstransfer.2023.124264.
[16] Yeranee, K., and Rao, Y., “A Review of Recent Investigations on Flow and Heat Transfer Enhancement in Cooling Channels Embedded with Triply Periodic Minimal Surfaces (TPMS),” *Energies*; Vol. 15, No. 23, 2022, p. 8994. doi: 10.3390/en15238994.
[17] Slater, J. W., “NPARC Alliance CFD Verification and Validation Web Site: CFD Varification and Validation,” https://www.grc.nasa.gov/WWW/wind/valid/tutorial/tutorial.html.
[18] Sain, C. K., Mathiazhagan, A., Bhapkar, S., Kazula, S., Asli, M., and Höschler, K., “Design Assessment and Test of Compact Gyroid-TPMS Heat Exchanger with Embedded Coolant Channels for LTPEM Fuel Cell Powered Regional Aircraft,” *DLRK 2025, Augsburg DE*.
[19] Sain, C. K., Haensel, J., Merbold, S., Schoen, F.-T., and Kazula, S., “Experimental Characterization of a Compact Gyroid-Pipe Heat Exchanger for Fuel Cell Powered Electric Aircraft Propulsion,” *The 15th EASN International Conference on “Innovation in Aviation & Space Towards Sustainability Today & Tomorrow”,* MDPI, Basel Switzerland, 2026, p. 78.
[20] DLR Institute of Electrified Aero Engines, “HEX 4 ELECTRA: Heat exchanger for electrified aero engines,” https://www.dlr.de/en/el/research-and-transfer/topics/hex-4-electra.
[21] SPALART, P., and ALLMARAS, S., “A one-equation turbulence model for aerodynamic flows,” *30th Aerospace Sciences Meeting and Exhibit,* American Institute of Aeronautics and Astronautics, Reston, Virigina, 1992.
[22] Menter, F. R., “Two-equation eddy-viscosity turbulence models for engineering applications,” *AIAA Journal*; Vol. 32, No. 8, 1994, pp. 1598–1605. doi: 10.2514/3.12149.
[23] Menter, F. R., Langtry, R., and Völker, S., “Transition Modelling for General Purpose CFD Codes,” *Flow, Turbulence and Combustion*; Vol. 77, 1-4, 2006, pp. 277–303. doi: 10.1007/s10494-006-9047-1.
[24] ANTJE LINK, and MARTIN STAGGAT, “Characterisation of thermal management specific heat rejection for electric propulsion architectures,” 2023.